Check for updates

www.advmattechnol.de

Tunable Mass Transport and Enhanced Electrochemical Performance of CO₂ Laser Engraved Electrodes

Davi M. De Farias, Gabriel N. Meloni,* and Thiago R. L. C. Paixão*

This work introduces a novel approach to laser-engraved electrochemical sensors by exploring vectorized CO2 laser engraving. Vectorized engraving reduces the interaction between the laser and the precursor material, decreasing uneven carbonization and enhancing charge transfer kinetics. The vectorized engraved patterns allow control over mass transport regimes. The final optimized electrode layout is a spiral, mimicking a disk electrode. Experimental and simulated evaluations have shown that diffusion can be modulated by adjusting the spiral spacing of the lines, leading to radial or planar diffusion. Comparative studies reveal that vector-engraved electrodes outperform raster-mode devices in current density (271 vs. 115–175 µA cm⁻²) and closely match commercial platinum electrodes (deviation (7%). Proofof-concept detection of levofloxacin confirms improved sensitivity without the need for post-fabrication treatments. Interestingly, the interdigitated electrodes incorporate the tunable mass transport features of the vectorized engraving method into numerical simulations to predict and optimize electrode design and electrochemical performance. This work establishes an alternative pathway for developing versatile, next-generation sensor platforms, overcoming the limitations of traditional laser engraving protocols.

1. Introduction

Electrochemical (bio)sensors are analytical tools developed to identify and quantify target molecules, spanning environmental, clinical, food, and forensic applications, especially in point-of-need scenarios. [1–3] Unsurprisingly, there is significant interest in developing new fabrication technologies that enhance scalability, reproducibility, and enable the decentralized production of these sensors. [4–6] Notably, cost-effective techniques, [7,8] including conductive inks, [7,8] 3D printed conductive thermoplastics, [9,10] and laser-engraving carbonization/pyrolysis of carbon sources [11–15] have been explored. Over the last decade, the use of lasers to convert non-conductive carbon into conductive carbon

D. M. De Farias, G. N. Meloni, T. R. L. C. Paixão
Departamento de Química Fundamental, Instituto de Química
Universidade de São Paulo
São Paulo 05508-000, Brazil
E-mail: gabriel.meloni@usp.br; trlcp@iq.usp.br

The ORCID identification number(s) for the author(s) of this article can be found under https://doi.org/10.1002/admt.202501374

© 2025 The Author(s). Advanced Materials Technologies published by Wiley-VCH GmbH. This is an open access article under the terms of the Creative Commons Attribution License, which permits use, distribution and reproduction in any medium, provided the original work is properly cited.

DOI: 10.1002/admt.202501374

has emerged as an alternative to traditional graphene domain production techniques, particularly over non-conductive carbon-based materials.[16-18] This process is driven by the interaction of photonic energy from a laser source with a carbon-based precursor material, initiating photothermal or photochemical processes, depending on the laser wavelength,[11,19] that lead to the conversion of sp³ into sp² carbon.^[20,21] The resulting carbonized surface morphology and physicochemical properties depend on the laser parameters, including power, scanning speed of the laser over the surface, number of laser passes, scan gap (the space between the laser path lines over the substrate), and the precursor material.[22-24] The electrochemical, and consequently analytical, response of these carbonized surfaces is normally subpar,[25-27] leading to the development of post-fabrication processes aimed at

improving the carbonized surface electrochemical and analytical response. $^{[28,29]}$

However, these additional procedures affect fabrication time and costs, decrease reproducibility,[30] limiting the application of laser-engraved electrodes. [22,31] Several efforts are being made to improve the electrochemical performance of the carbonized surfaces[32-34] broadly focusing on 3 aspects: i) laser type, ii) carbon precursor material, and iii) laser parameters. [35,36] Aspects i and ii are set before the experiment, and lay the ground for the electrochemical performance, as the laser wavelength will bias toward either photothermal or photochemical process to convert non-conductive carbon to conductive carbon. The precursor material will set the amount and hybridization of the starting carbon material, which will impact on the final electrochemical performance of the carbonized surface. [37,38] Aspect iii allows for flexibility during the experiments, as multiple laser parameters (see above) can be modified to tailor the electrochemical performance. [39,40] Several reports attempt to find a correlation between fabrication parameters and electrochemical performance,[31,36,41] worth noting is Murray et al. work that have developed a response surface model that integrates the effects of scan speed and laser power on the electrochemical performance of carbonized surfaces. Their findings led to a non-linear model, illustrating the intricate interactions that occur during the engraving process.^[30] Chyan et al. work evaluated the effects of repeating the engraving process in the same area and adjusting the focal distance. The multiple laser exposures produced an



www.advancedsciencenews.com

ADVANCED
MATERIALS
TECHNOLOGIE

www.advmattechnol.de

intermediate phase of amorphous carbon, which favors the formation of graphene on the surface, thereby improving electrical conductivity.^[20]

Despite the numerous efforts, it is evident that due to the complex nature of the interaction between the laser and the sample, and the interconnected fabrication parameters, establishing a clear cause-and-effect relationship directly linking fabrication and electrochemical response is challenging.[11] Numerous studies are contradictory regarding the engraving conditions and their impact on the carbonized surface properties, including the electrochemical response, which leads to a lack of reproducibility among experiments and different laboratories.[20,24,30,40] In this work, to better understand the carbonized surface electrochemical performance and its analytical applicability, we take efforts to minimize the interactions between the many instrumental parameters, mainly focusing on the effect of scan gap (aspect iii) during the fabrication of electrodes using the vectorized engraving mode. [31,41] We focused on using a CO_2 laser (aspect i) and phenolic paper as the carbon-containing substrate (aspect ii). Our approach is stepwise, first understanding the electrochemical response of a single line, and then multiple lines and the interplay between the scan gap (the distance between the lines) and mass transport regimes at carbonized surfaces. We show that controlling a single parameter within aspect iii allows us to fine tune the diffusion regime toward the electrode surface, better than using raster mode, [31,42] and is enough to fabricate carbonized surfaces that are better performing, in terms of reversibility of the electrochemical process, for some molecules. We reason that this is due to exposing the surface only briefly to the laser, which decreases the number of complex interactions happening over the surface.

2. Results and Discussion

Laser engraving can be categorized into two techniques: raster and vector. Raster engraving operates similarly to an inkjet printer, where the laser moves back and forth across the material, gradually engraving individual lines to construct the design. The resolution-typically measured in scan gap or dots per inchdirectly impacts the final engraving quality. A higher resolution corresponds to a smaller scan gap, resulting in engraved lines positioned closer together. In contrast, vector engraving follows pre-defined vector paths rather than scanning the entire surface. Instead of filling an area with closely spaced lines, the laser only traces the outline of a design, in a continuous motion.^[43] If a surface is to be carbonized entirely with vector engraving, the drawing of the surface needs to include lines within the surface outline. As such, the scan gap in a vector engraved surface can also be controlled, but not in the laser software, but by drawing lines, spaced by a given amount (scan gap), within the outline of the surface to be engraved. Raster engraving is usually employed for fabricating electrodes, as it allows for filling a predefined area with carbonized material, forming an electrode surface.[11,20,41] At small scan gaps for both vector and raster engraving, smaller than the laser beam spot over the surface, engraving a design can lead to partially overlapping lines, which means that different areas of the carbonized surface were subject to varying amounts of interaction with the laser. This truly complicates the reasoning of any relation between fabrication parameters and the electrochemical response of the carbonized surface, as another degree of heterogeneity is added to the surface composition. Ideally, one way to remove this added complication would be to fabricate a carbonized surface formed by lines with zero spacing between them. This is why we will focus on vector engraving for producing carbonized surfaces, as it provides fine control of the space between the engraved lines by drawing lines with different spacing between them. With prior knowledge of the carbonized line width, which can be accessed by optical microscopy, this can be done accounting for line width, allowing for the proper control of inter-line spacing and the scan gap.

2.1. Scan Gap Impact on the Electrode Response

To evaluate the effects of scan gap on electrode response, we first resort to the raster engraving mode, which is most often used. The effects of scan gap on a carbonized surface are multifactorial, from the complication of generating a surface with heterogeneous interactions with the laser, to simple issues with electrical resistance. Overlapping engraved lines, or lines apart but with different lengths, could lead to heterogeneous electrical conductivity across the electrode surface, which would impact the electrochemical response. First, we evaluate how the laser scanning orientation, in the XY plane, and scan gap affect the electrical conductivity of the carbonized surface. The experiments were conducted using a test device outlined in Section \$1.1 (Supporting Information) (Figure \$4A Supporting Information). Figure \$4D (Supporting Information) shows that electrical resistance rises with scan gap from 25 to 500 μ m, yielding 18.75 to 210.83 Ω for the X-axis and 17.74 to 184.40 Ω for the Y-axis. The surface resistance measurement protocol is described in Section S4 (Supporting Information). As the electrical resistance is measured across the X-axis, engraving lines parallel to this axis maintain electrical contact regardless of the space between engraved lines. In contrast, when lines are engraved along the Y-axis, at a scan gap of 500 µm, there is a lack of electrical contact. It is evident that small line spacings result in lower electrical resistance, [44] which could favor the electrochemical response of an electrode, but at these smaller spaces, lines are overlapping, which, as mentioned before, could impact the electrochemical response.

To evaluate how scan gap affects the electron transfer kinetics of the carbonized surface, we utilize $[Ru(NH_3)_6]^{3+}$ as a nonsurface-sensitive redox probe. As illustrated in **Figure 1A**, working electrodes were fabricated, consisting of a 6 mm diameter disk, comprised of multiple lines with the scan gap ranging from 25 to 200 μ m in raster-engraving mode, as detailed in Section S1.2 (Supporting Information). The cyclic voltammograms (CVs) portrayed in Figure 1C, recorded with scan gaps of 100 (blue trace) and 200 μ m (green trace), exhibit quasi-reversible behavior, characterized by anodic and cathodic peaks with similar absolute current values (Figure 1D, gray bars), and a peak potential separation (Δ E) smaller than 65 mV (Figure 1D, green bars).

Electrodes fabricated with a scan gap of 25 μm (brown trace) and 50 μm (gray trace) exhibit decreased ratios of anodic and cathodic peak currents and increased ΔE values, indicating a shift toward an irreversible voltammetric profile. It is also worth noting that, as the disk diameter is constant, larger scan gaps mean less surface covered by carbonized material, which should

and-conditions) on Wiley Online Library for rules of use; OA articles are governed by the applicable Creative Commons

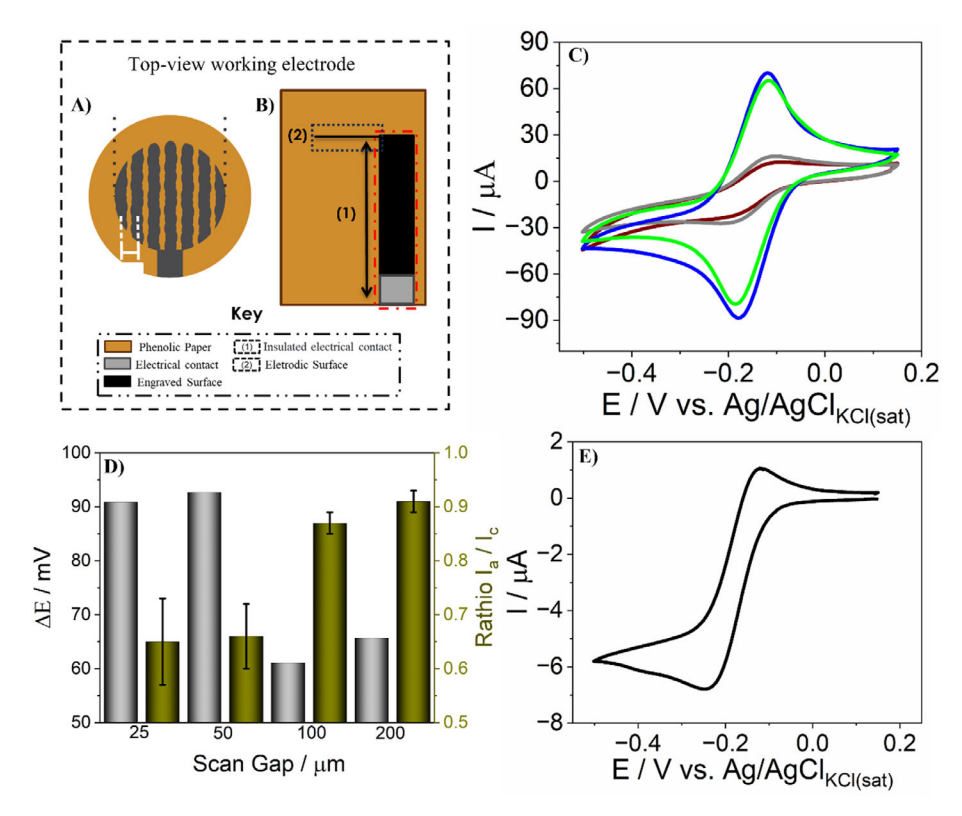


Figure 1. A) Schematic illustration of the disk working electrode engraved at raster-mode. B) Schematic illustration of a single line working electrode engraved at vector-mode. C) CVs recorded (scan rate: 25 mV s⁻¹; n = 3) with [Ru(NH₃)₆]⁺³ (5.0 mmol L⁻¹ in 0.5 mol L⁻¹ KCl) with the fabricated electrodes. Scan gap – 25 μm (brown trace); 50 μm (gray trace); 100 μm (blue trace) and 200 μm (green trace). D) Peak potential separation (ΔE) values (gray bars) and anodic and cathodic peak current ratios (green bars) for the voltammograms in panel C. E) CV recorded with [Ru(NH₃)₆]⁺³ (5.0 mmol L⁻¹ in 0.5 mol L⁻¹ KCl) onto single line working electrode (scan rate: 5 mV s⁻¹; n = 3) engraved at vector-mode. Laser engraving conditions: Raster mode; power = 2.0 W, scanning speed = 8.8 mm s⁻¹, focal distance = 12.0 mm, and scan gap = 25, 50, 100, and 200 μm. Vector mode: power = 0.7 W, scanning speed = 30.0 mm s⁻¹, and focal distance = 12.0 mm, pace number = 4 times.

result, if there is no diffusional overlap between the lines, [28,32] in smaller recorded currents then electrodes with smaller spacing, and hence a larger amount of surface covered with carbonized materials. The fact that we are seeing the complete opposite aligns with the lack of reversibility in the voltammetric profile and suggests that small scan gaps, with overlapping carbonized lines, result in a surface with slower electron transfer kinetics for [Ru(NH₃)₆]³⁺. The depth of the carbonized layer on the phenolic substrate was assessed for various scan gaps (fully described in Section S5, Supporting Information), resulting in depths of 400, 150, and 100 µm for scan gaps of 50, 100, and 200 µm, respectively (Figure S5, Supporting Information). These results highlight how, at smaller gaps, there is overlap between the lines, resulting in the surface being carbonized multiple times, increasing the interaction between the laser and the surface. At least for [Ru(NH₃)₆]³⁺, this increased interaction results in a slower electron transfer rate, alluding to the complexity of the laser/precursor material interaction.

2.2. Electrochemical Response of Single and Multiple Lines

As overlapping lines can jeopardize the electrochemical response of an electrode, we seek to understand the electrochemical response of a single line. For such, we resort to the vector engraving mode, controlling the scan gap by drawing spaced lines. We adjusted the laser scanning speed to achieve the thinnest possible line. Unfortunately, this turned out to be quite challenging, as increasing speed resulted in lines that were not entirely connected/carbonized, without continuous electrical connection over the entire length, a limitation due to aspects i and ii (see above). We found a compromise between increasing speed and engraving the same line multiple times, here 4 times, which resulted in lines with 100 μm in width and 20 μm in depth (Figures S1B and S5D, Supporting Information). Even though we are engraving a line multiple times, similarly to overlapping lines, the interaction time between the laser and the precursor material is far reduced due to the faster scan speeds, marked by the shallow line depth, which, as we will see results in surfaces with similar electron transfer rates as those reported in the literature for laser-engraved electrodes. Further details about the fabrication protocol are outlined in Section \$1.3 (Supporting Information). To investigate the response of a single line, we set for the electrode dimensions 4.5 mm in length (Figure 1B). The voltammetric profile of [Ru(NH₃)₆]³⁺ for the single line can be seen in Figure 1E, where a clear shift toward a sigmoidal profile is seen, like a band-microelectrode, showing the influence of radial diffusion on the voltammetric profile. Leveraging radial diffusion, it is

and-conditions) on Wiley Online Library for rules of use; OA articles are governed by the applicable Creative Commons License



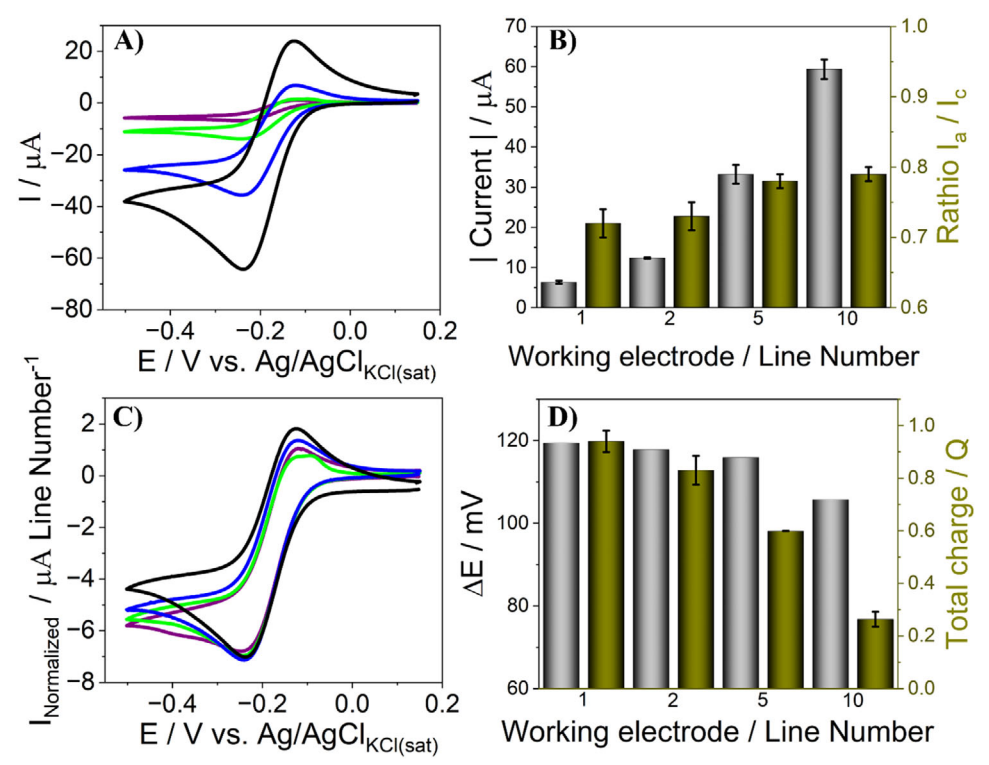


Figure 2. A) CVs were recorded (scan rate: 5 mV s^{-1} ; n = 3) with $[Ru(NH_3)_6]^{+3}$ (5.0 mmol L^{-1} in 0.5 mol L^{-1} KCl). Number of lines: 1 (purple trace), 2 (green trace), 5 (blue trace), and 10 (black trace). B) Absolute value of the cathodic current (gray bars) and the ratio of anodic to cathodic peak currents (green bars) for the voltammograms in panel A. C) Voltammograms in panel A normalized by the number of lines in each electrode. D) ΔE values (gray bars) and Total charge (green bars) for the voltammograms in panel A.

possible to fabricate electrodes with multiple lines (Figure S2A, Supporting Information) and adjust the scan gap, accounting for the line width, to a situation where there is diffusional overlap between them, favoring an overall linear diffusion toward the electrodic surface. [46]

Figure 2A displays the CVs profiles of working electrodes with 1, 2, 5, and 10 lines with a scan gap of 100 µm. It should be noted that this scan gap considers the line width and reports the distance between the edges of each engraved line. The Faradaic peak currents increase linearly with the number of carbonized lines (Figure 2B, gray bars). As the number of traces on the working electrode surface increases, the ratio of anodic to cathodic currents moves toward unity (Figure 2B, green bars), pointing to an increased contribution of linear diffusion to the overall mass transport resulting from the diffusional overlap between the lines. Figure 2C displays the voltammograms normalized by the number of individual lines, demonstrating that each trace contributes equally to the faradaic current. Despite the increased ΔE values (Figure 2D, gray bars), which may result from the increased electrical resistance from the length of the multiple lines, the values still align with those found in the literature for CO_2 laser-engraved electrodes, where ΔE values remain below 120 mV.[47] Figure 2D (green bars) shows the normalized charge flow in the system, resulting from integrating the voltammograms normalized by the cathodic peak current over time. More information regarding this parameterization can be found in Section \$6 (Supporting Information). The total charge decreases as the number of individual lines increases. For linear diffusion,

near-zero values of charge are expected. The trend in Figure 2D supports the increased linear diffusion contribution to the overall mass transport.

The increase in linear diffusion toward the electrodes is clear, resulting from the diffusional overlap between the engraved lines, which can be tailored by adjusting the scan gap (more information is outlined in Section \$1.3, Supporting Information). Experiments were conducted with working electrodes with ten engraved lines (Figure S2, Supporting Information) with scan gaps of 100, 200, 500, and 1000 $\mu m.$ The voltammogram profile (Figure 3A) exhibits a clear shift in mass transport regime with the change in scan gap. At 1000 µm, the electrode behaved as an array of independent band microelectrodes (Figure 3A, purple trace), whereas reducing the distance toward 100 µm induced overlapping diffusion layers, shifting the mass transport toward planar diffusion (Figure 3B) and yielding a peak-shaped voltammogram (Figure 3A, black trace).[46] This transition is corroborated by numerical simulations performed with the designed electrode geometry. Figure 3B, in the top panel, shows the simulated diffusion profile over a series of lines 100 µm apart, taken at the most negative potential of a simulated voltammogram. There is a significant overlap of the diffusion layers, marked by the predominantly flat diffusion profile. Contrary, at a scan gap of 500 µm (Figure 3B, bottom panel), at the same simulation conditions, there is almost no diffusional overlap, and each line behaves as an independent band microelectrode. This is further supported by the increase in total normalized charge (Figure 3C). A normalized charge of 1 would mean a perfectly

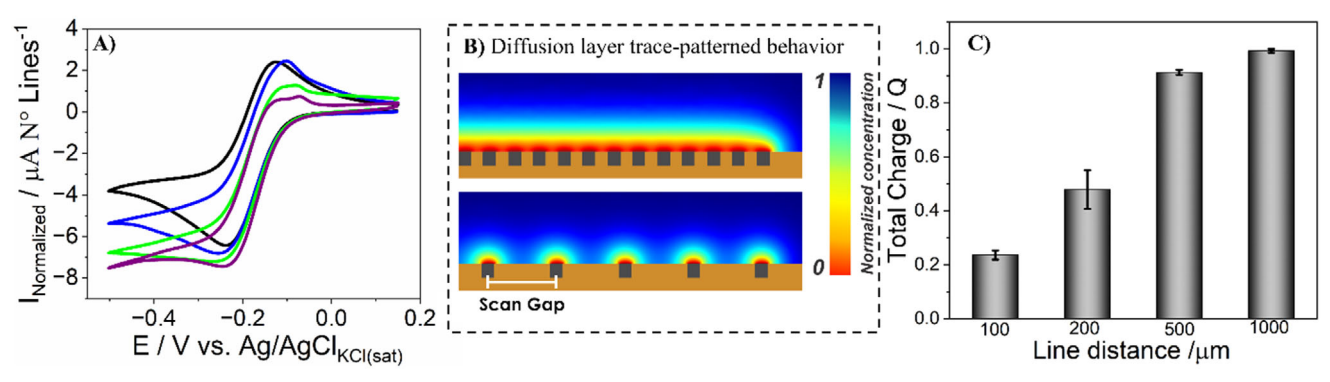


Figure 3. A) CVs were recorded (scan rate: 5 mV s⁻¹; n = 3 with $[Ru(NH_3)_6]^{+3}$ (5.0 mmol L⁻¹ in 0.5 mol L⁻¹ KCl). Scan gap of 100 μ m (black trace), 200 μm (blue trace), 500 μm (green trace), and 1000 μm (purple trace). B) Simulated Diffusion layer profile for working electrode at 100 μm and 500 scan gap. C) Total charge for the voltammograms in panel A.

sigmoidal voltammogram, which is seen for line spacings of 500 and 1000 µm, with the 500 µm one corroborating with the diffusion profile seen in the simulation (Figure 3B, bottom panel).

2.3. Vector-Engraved Disk Electrodes

We have demonstrated that it is possible to fabricate an array of band microelectrodes with tunable inter-electrode spacing (scan gap) using laser engraving, which directly affects the diffusion regime of species toward the electrode surface. It is worth noting that mass transport and, in fact, microband electrodes, can be fabricated using raster engraving mode if the true line spacing is known and accounted for, which essentially transforms raster and vector engraving in similar procedures. [48,49] Using raster engraving mode, arrays of microbands have been reported, but they are usually rectangular in nature, which can find applications, [50] but a much more common geometry for working electrodes is disk-shaped electrodes. Although this geometry may seem challenging to reproduce with lines, it can be achieved with a single vector engraved line, in the form of a spiral (Figure 4A). If the interline spacing is enough to result in complete diffusional overlap between the spiral lines, a single band microelectrode can be made to act as a disk electrode. For drawing the electrode, we used CorelDraw symmetric spiral tool, which generates a spiral like an Archimedes spiral. The outer diameter of the spiral was set 6 mm and the line spacing is adjusted by changing the number of lines within the spiral. One consequence of this geometry is that the engraved electrode is very resistive (Figure S7A, Supporting Information, red trace). A single band microelectrode has a length of 4.5 mm, while the spiral has a length of approx. 13 cm.^[51] To overcome the ohmic drop limitation seen in the voltammograms, we included a "crosshair" centered in the spiral, connecting the multiple lines of the spiral, thus reducing the overall resistance (Figure S7A, Supporting Information, black trace). The Section S7 (Supporting Information) includes details of electrode fabrication characterization.

Spiral electrodes featuring scan gaps of 100, 200, 500, and 1000 μm (Figure S8A,B, Supporting Information) were assessed byCV using $[Ru(NH_3)_6]^{3+}$ as a redox probe. Experiments were performed at two voltammetric scan rates, 5 (Figure S8C, Supporting Information) and 50 mV s⁻¹ (Figure S8D, Supporting In-

Adv. Mater. Technol. 2025, e01374

formation). At both scan rates, the trend of increased linear diffusion contribution to mass transport with decreasing scan gap is evident, as indicated by the increased cathodic/anodic peak current ratio (Figure S8E,F, Supporting Information, green bars), which approaches 1 for the smallest gap (100 µm). Peak potential separation for all cases (Figures S8C,D, Supporting Information) remains larger than expected for the reversible case, despite employing ohmic-drop compensation. This suggests that there must be a kinetic limitation in the voltammogram. From gaps of 100 to 1000 μm , ΔE values of 98.1 to 117.5 mV at a scan rate of 5.0 mV s⁻¹ (Figure S8G, Supporting Information, green bar) and 80.3 to 97.7 mV at 50 mV s⁻¹ (Figure S8H, Supporting Information, green bar) were observed. The increase in diffusional overlap is also evident if we compare the peak currents for the expected diffusion-limited currents, at the same conditions, of a 6 mm diameter (0.283 cm²) with the ones obtained experimentally (Figure S8E,F, Supporting Information, gray bars). When we normalize the experimental currents by the theoretical one, values ranged from 97% to 18% at $5.0 \,\mathrm{mV \, s^{-1}}$ (Figure S8G, Supporting Information, gray bar) compared to 79% to 33% at 50 mV $\rm s^{-1}$ (Figure S8H, Supporting Information, gray bar) for scan gaps of 100 to 1000 μm . The diffusional overlap is once more corroborated by simulations of the spiral electrode geometry at the voltammetric scan rate of 5 mV s⁻¹ (Figure 4B), with the voltammetric profiles closely matching.

2.3.1. Spiral Electrode versus Disk Electrode

Figure 4C presents the [Ru(NH₃)₆]³⁺ voltammetric profiles of the spiral electrode (black trace) compared to 6 mm diameter disk laser engraved electrodes fabricated using common laser parameters^[52] and the raster mode (see Section S1, Supporting Information). The disk electrodes fabricated using the raster mode had scan gaps of 50, 100, and 200 µm. At the fabrication conditions, the smallest line produced in the raster mode is 300 µm (Figure S1, Supporting Information). Increasing the gap in raster mode from 50 to 200 µm (gray, green, blue traces - Figure 4C) improves the electrochemical response, marked by an increased peak current density and a decreased current deviation from the theoretical value for a 6 mm disk electrode, with increasing the line spacing (Figure 4D). At 50 μm gap, the

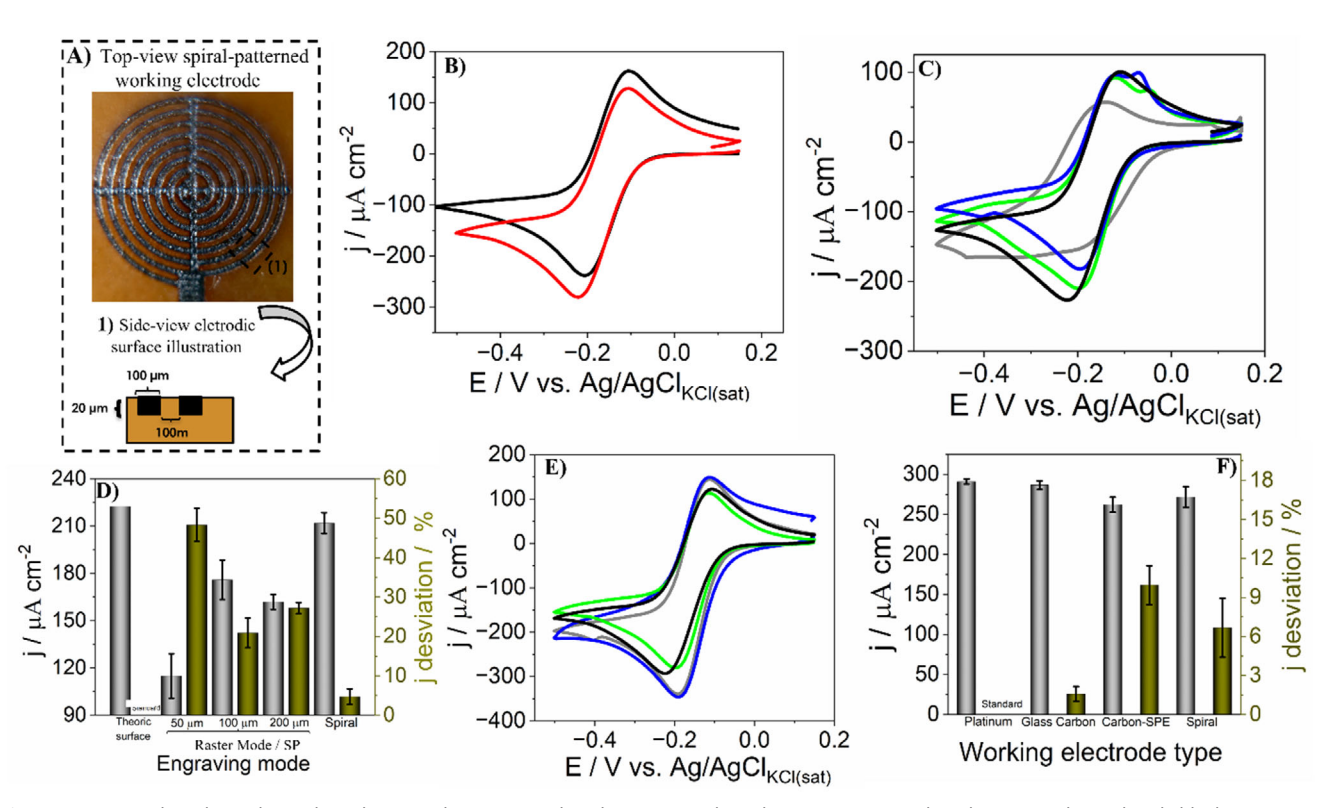


Figure 4. A) Spiral working electrode with a crosshair engraved under vectorized mode. B) Experimental (red trace) and simulated (black trace) CVs (scan rate: 5 mV s; n = 3) recorded with [Ru(NH₃)₆]⁺³ (5.0 mmol L⁻¹ in 0.5 mol L⁻¹ KCl). C) CVs profile comparison of raster-engraved [50 μm, gray trace; 100 μm, blue trace; and 200 μm, green trace; scan gaps] working electrodes and vector engraved (spiral, black trace) working electrode. D) Current density (gray bars) and current density deviation from an ideal disk electrode (green bars). E) CV profile of spiral (black trace) versus commercial [platinum, blue trace; glassy carbon, gray trace; SPE-carbon, green trace] working electrodes. F) Current density (gray bars) and its corresponding deviation (green bars) from a Platinum working electrode.

lowest current density of 115 μA cm $^{-2}$ (48% deviation from ideal disk electrode values) was observed, while increasing the gap to 100 and 200 μm improved performance to 175 μA cm $^{-2}$ (20% deviation) and 161 μA cm $^{-2}$ (27% deviation), respectively. We reason that the performance increase of the raster-engraved electrodes is related to the decrease in overlap between the engraved lines. As the parameters in the raster mode result in lines of 300 μm (Figure S1A, Supporting Information), and the scan gap in the laser software is measured at the center of the engraved line, even with a scan gap of 200 μm and a line of 300 μm , there is roughly 100 μm of overlap between the lines.

The results portrayed in Figure 4C,D support our assumption that increased laser interaction results in an electrodic surface that is less conducive to the $[Ru(NH_3)_6]^{3+}$ redox cycling. The spiral electrode presented the highest current density, 211 µA cm⁻², representing only 5% deviation of the expected current of a disk electrode (Figure 4D, green bars). Despite having only 50% of the 6 mm area covered by carbonized lines, the spiral electrode behaves more like a disk electrode than a completely carbonized 6 mm diameter disk electrode. One great advantage of using the spiral design is in the fabrication time (see the support video). A single 6 mm disk electrode, fabricated by raster engraving, takes 6.5 s, while a single spiral elec-

trode takes 3.2 s. By using vector engraving and a spiral design, we can fabricate electrodes that perform better and are twice as fast to manufacture as conventionally fabricated laser-engraved electrodes.

In Figure 4E, we also compare the voltammetric profile of the spiral electrodes (black trace) against that of commercial 2.0 mm diameter platinum (blue trace), 1.5 mm diameter glassy carbon (gray trace), and 4.0 mm diameter carbon screen printed – SPE (green trace) disk electrodes. The current density analysis in Figure 4F (gray bars) shows that commercial electrodes displayed current densities ranging from 262 to 291 $\mu A\ cm^{-2}$ with platinum having the highest value, followed by glassy carbon and carbon SPE. The spiral electrode displayed a current density of 271 µA cm⁻², over-performing the SPE-electrode. Deviation analysis of the current density showed minimal variation from the platinum electrode, taken as the standard, with glassy carbon at 1.5%, SPE at 9.9%, and the spiral electrode at 6.8% (Figure 4F, green bar). These results confirm that the spiral electrode surface behaves similarly to a disk electrode, demonstrating electrochemical performance comparable to that of commercial systems, remarkably resembling that of SPE,[54] despite having a higher D/G ratio in comparison to the SPE-carbon electrode surface (see Section S8 and Figure \$9, Supporting Information).

conditions) on Wiley Online Library for rules of use; OA articles are governed by the applicable Creative Commons

300-A)

225

150

75

0

0.4

10 D)

0

-20

-30

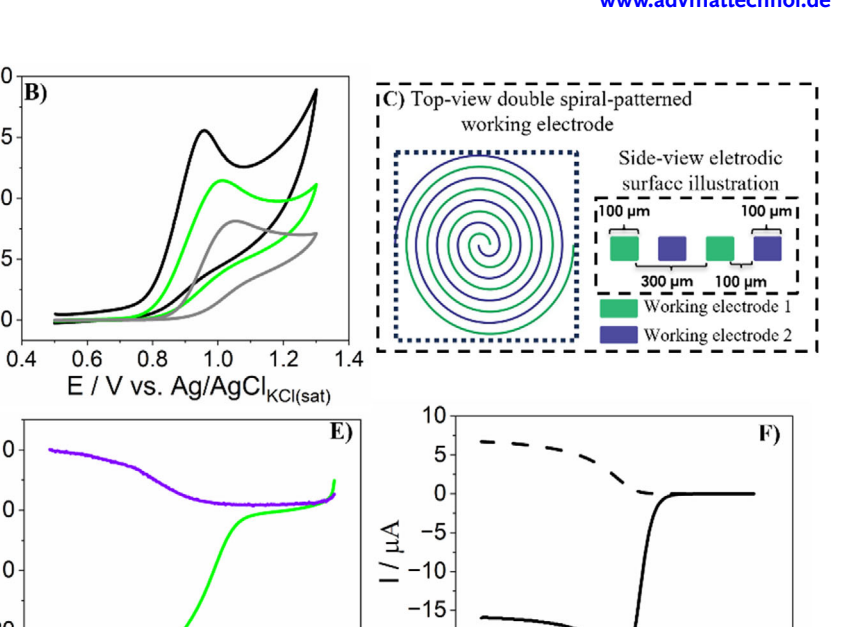
0.8

1.0 E / V vs. Ag/AgCl_{KCl(sat)}

-0.8 -0.6 -0.4 -0.2 0.0 0.2 0.4

E / V vs. Ag/AgCl_{KCl(sat)}

j / μΑ cm⁻²



-20 -25

Figure 5. A) CVs were recorded (scan rate: 5 mV s⁻¹; n = 3) in the presence of LEV (1.0 mmol L⁻¹ in 0.04 mol L⁻¹ BR buffer -pH 6), comparing the engraving mode: raster [50 µm, gray trace; 100 µm, blue trace; and 200 µm, green trace)/scan gap] and vector-engraved (spiral-, black trace). B) CV's profile of spiral (black trace) versus commercial [glassy carbon, gray trace/SPE-carbon, green trace] working electrodes for LEV oxidation process. C) Top-view and cross-sectional schematic of interdigitated spiral working D) CVs (scan rate: 5 mV s⁻¹; n = 3) recorded in the presence of [Ru(NH₃)₆]⁺³ (5.0 mmol L-1 in 0.5 mol L-1 KCl) onto the interdigitated working electrode (working electrode 1, purple trace/working electrode 2, green trace). E) Experimental and F) simulated Generator/collector CVs recorded in the presence of $[Ru(NH_3)_6]^{+3}$ (5.0 mmol L⁻¹ in 0.5 mol L⁻¹ KCl). Generator/collector Experimental conditions- Generator (working electrode 1): scan rate: 2 mV s⁻¹; potential range: +0.3 to -0.8 V; Collector (working electrode 2): Ep: 0.4 V; acquisition time: 600 s

-0.8 -0.6 -0.4 -0.2 0.0 0.2 0.4

E / V vs. Ag/AgCl_{KCl(sat)}

300

225

150

75

0

10

0

-30

j/μA cm⁻²

2.3.2. Spiral Electrode: A Suitable Analytical Tool

Having demonstrated the electrochemical behavior of the spiral electrode with an outer-sphere redox probe, we now focus on the electrochemical performance of the electrode toward the oxidation of levofloxacin, a fluoroquinolone antibiotic increasingly recognized as an environmental contaminant, and an important analyte for sensing applications, [55] and that is notorious for adsorbing in electrodic surfaces.[56,57] While numerous sensors have been developed for levofloxacin (LEV) detection, most existing designs require complex fabrication protocols or extensive surface modifications.^[58,59] Figure 5A shows the LEV oxidation process on the spiral electrode (black trace) and 6 mm diameter raster engraved electrodes with scan gaps of 50 µm (gray trace), 100 µm (blue trace), and 200 µm (green trace). As before, increasing scan gap resulted in increased current density from 82 to 185 μA cm⁻² over the scan gap range. For the spiral electrode, a current density of 265 µA cm⁻² was found, coupled to an enhanced voltammetric peak definition (Figure 5A, black trace). These results suggest, once more, that raster engraving with overlapping lines has a detrimental impact on the electron transfer kinetics at the electrode surface, which we have seen for outer-sphere species and are now seeing for LEV. Even when compared to commercial electrodes (Figure 5B), in terms of current density, the spiral electrode (black trace) outperforms a glassy carbon (gray trace) and carbon SPE (green trace) electrodes by 1.4 and 2.1 times, respectively. This performance can be attributed to the larger surface area of laser-engraved electrodes when compared to glassy carbon, which favors the oxidation of LEV as the molecule adsorbs on the electrode's surface. [60] Interestingly, SPE electrodes also have a larger surface area when compared to their geometric area, and the better performance of the spiral electrode, when compared to the SPE electrode, can be at least partially attributed to better electron transfer kinetics at the spiral electrode surface.

-0.8 -0.6 -0.4 -0.2 0.0 0.2 0.4

E / V vs. Ag/AgCI_{KCI(sat)}

The vector engraved electrode design simplicity and the ability to tune the mass transport over the electrode can be explored to create new electrode designs. For instance, Archimedes spirals, when drawn in opposition, can be nested together, with one spiral occupying the space between the lines of the other. With these, we can create interdigitated spiral electrodes, which maintain the disk shape (Figure 5C) and can be used independently or in tandem in a generation/collection mode. Our design keeps the 100 µm line spacing between the lines of spiral one (green) and spiral two (purple). One at a time, each of the spiral electrodes was characterized by CV in [Ru(NH₃)₆]³⁺ solution (Figure 5D), with both voltammograms overlapping, demonstrating that the two spirals are identical. Simulated voltammograms for each of the spirals match the experimental maximum cathodic current values (Figure \$10A, Supporting Information). Moreover, the slanted profile of the voltammograms reveals the resistive nature of the electrode, as the length of each spiral line is 7 cm. Mitigating this resistance by using the "crosshair", as done

www.advancedsciencenews.com



www.advmattechnol.de

for the spiral electrode, is more challenging due to the nested geometry, and we opted not to implement it. The electrodes were also tested in a generation/collection configuration, with each spiral alternating as generator and collector (Figure 5E; Figure S10C, Supporting Information) at a scan rate of 2 mv s $^{-1}$ (see Section S8 and S10B, Supporting Information). As expected, the collection efficiency is similar in both configurations, as both electrodes are nearly identical (Figure 5D). A collection efficiency of $38.0\pm3\%$ is observed in both cases, deviating by only 4% from the simulated collection efficiency of 42% (Figure 5F). The use of a generation/collection setup is beneficial for analytical applications, allowing for the indirect monitoring of analytes that are not electroactive but react with molecules that enable the conditioning of the sensing area to increase sensitivity and remove interfering species. $^{[61]}$

3. Conclusion

This study presents a novel fabrication protocol for electrodes using a CO2 laser engraving in the vector-mode, which overcomes the limitations of conventional raster-mode laser engraved electrodes electrochemical responses. Through experiments and numerical simulations, we establish a solid framework for designing sensors with predictable and tunable electrochemical behavior. By systematically altering the inter-line distance in spiral electrodes, we were able to modulate the mass transport toward the electrode surface, favoring either planar or radial diffusion. When planar diffusion was favored, the 6 mm outer diameter spiral electrode presented current densities closer to theoretical values than similar-sized disk electrodes made by raster-mode. This protocol is flexible, enabling its application with different precursor materials, and should support the development of customizable electrochemical platforms for a wide range of applications. Additionally, combining vector-mode laser engraving with numerical simulations opens the path for developing customized electrochemical interfaces by affording a predictive insight into the electrode performance before it is even fabricated. Future research could investigate other geometric configurations and material combinations to broaden the applicability of this approach.

4. Experimental Section

Reagents and Materials: All solutions were prepared using deionized water with a resistivity of 17.5 $M\Omega$ cm, obtained from a Millipore Direct-Q 5 purification system. Potassium chloride (KCl), 99.5%; boric acid (H $_3$ BO $_3$), 98.0%; and glacial acetic acid (CH $_3$ COOH) were obtained from Merck. Hexaamminerruthenium(III) chloride [Ru(NH $_3$) $_6$ Cl $_3$] and Levofloxacin (99.0%) were obtained from Sigma–Aldrich. Phosphoric acid (H $_3$ PO $_4$) 85.0% was purchased from Vetec.

Phenolic paper, Silver conductive ink PC-9070/1, and transparent nail polish were acquired from Pertech (São Bernardo do Campo, Brazil), Joint Metal Ltda (Diadema, Brazil), and local stores, respectively.

Electrodes Layout and Fabrication: Electrodes were fabricated via CO_2 laser engraving carbonization in both raster and vector mode. For most electrodes, parameters established in previous studies by our research group were used: $^{[29]}$ power =2.0 W, scanning speed =8.8 mm s $^{-1}$, focal distance =12.0 mm, and scan gap $=25,\,50,\,100,$ and $200\,\mu m.$ For the spiral electrodes and derived electrode designs, the parameters used were power =0.7 W, scanning speed =30.0 mm s $^{-1}$, and focal distance =12.0 mm. For these electrodes, the engraving procedure is repeated four times over the same spot to form continuous carbonized lines. Electrical

contacts from the carbonized surfaces to the connection leads of a potentiostat were coated with conductive silver ink to minimize resistance and isolated from solution contact using a commercial nail polish insulating layer. Electrode designs were created in CorelDRAW. The Supporting Information provides detailed specifications regarding the working electrode design and corresponding instrumental parameters (Section S1, Supporting Information).

Electrochemical Measurements: Electrochemical measurements were performed using a Metrohm Autolab PGSTAT 128N and a PGSTAT 204 potentiostat/galvanostat. Both were controlled using the software NOVA 2.1.7, which was responsible for data collection and processing. Evaluation of the carbonized surfaces electrochemical performance was made by CV in a KCl medium containing $[Ru(NH_3)_6]^{3+}$ as a redox probe or in a BR buffer (pH 6) containing LEV. More details regarding standard solution preparation are provided in Section S2 (Supporting Information). CV and linear voltammetry were employed to characterize the engraved interdigitated working electrode layout in generator/collector mode, using $Ru[(NH_3)_6]^{3+}$ as a redox probe. The measurements were conducted in triplicate, and the CVs portrayed in the figures are the average (n=3) of raw data.

Numerical Simulations: Finite element method simulations were performed in COMSOL Multiphysics (v6.2) using the transport of diluted species module. A 2D axisymmetric geometry was used for all simulations of the spiral and interdigital electrode geometries. Butler-Volmer kinetics was used to simulate $[{\rm Ru}({\rm NH_3})_6]^{3+}$ cyclic voltammograms at different scan rates, according to the experimental framework. A large k^0 value (10 cm s $^{-1}$) was assumed due to the fast electron transfer rate of the outer-sphere redox probe $[{\rm Ru}({\rm NH_3})_6]^{3+}$ on carbon. Similarly, the transfer coefficient (α) was assumed to be 0.5. More details on the simulations, including the simulation domain geometry and boundary conditions, are provided in Section S3 (Supporting Information).

Supporting Information

Supporting Information is available from the Wiley Online Library or from the author.

Acknowledgements

This research was supported by the São Paulo Research Foundation (FAPESP) (Grant Nos. 2023/00246-1 and 2021/00800-3), and Conselho Nacional de Desenvolvimento Científico e Tecnológico (CNPq) (Grant Nos. 302839/2020-8, 405620/2021-7, 465389/2014-7, and 140463/2021-6). This study was financed in part by the Coordenação de Aperfeiçoamento de Pessoal de Nível Superior – Brasil (CAPES) – Finance Code 001, Program 33002010191P0.

Conflict of Interest

The authors declare no conflict of interest.

Author Contributions

DM.d.F. was responsible for the methodology, formal analysis, investigation, and writing of the original draft. G.N.M. contributed to the conceptualization, supervision, investigation, and writing—review and editing. T.R.L.C.P. was involved in conceptualization, supervision, resource provision, project administration, funding acquisition, and writing—review and editing.

Data Availability Statement

The data that support the findings of this study are available from the corresponding author upon reasonable request.

2365709x, 0, Downloaded from https:

advanced.onlinelibrary.wiley.com/doi/10.1002/admt.202501374 by University Of Sao Paulo - Brazil, Wiley Online Library on [18/09/2025]. See the Terms

conditions) on Wiley Online Library for rules of use; OA articles are governed by the applicable Creative Commons

Keywords

disk-electrode, electrode fabrication, microelectrode array, numerical simulations, planar diffusion

> Received: June 27, 2025 Revised: August 19, 2025 Published online:

- [1] J. Heikenfeld, A. Jajack, J. Rogers, P. Gutruf, L. Tian, T. Pan, R. Li, M. Khine, J. Kim, J. Wang, J. Kim, Lab Chip 2018, 18, 217.
- [2] G. Alarcón-Angeles, G. A. Álvarez-Romero, G. Rosati, C. Parolo, A. Merkoçi, in Encyclopedia of Sensors and Biosensors, 1st ed, (Ed.: R. Narayan), Elsevier, Oxford 2023, pp. 772.
- [3] F. R. Simões, M. G. Xavier, in Nanoscience and Its Applications (Eds.: A. L. Da Róz, M. Ferreira, F. de Lima Leite, O. N. Oliveira), William Andrew Publishing, Norwich, NY 2017, pp. 155.
- [4] J. Wu, H. Liu, W. Chen, B. Ma, H. Ju, Nat. Rev. Bioeng. 2023, 1,
- [5] S. K. Krishnan, E. Singh, P. Singh, M. Meyyappan, H. S. Nalwa, RSC Adv. 2019, 9, 8778.
- [6] M. Baharfar, M. Rahbar, M. Tajik, G. Liu, Biosens. Bioelectron. 2020, *167*, 112506.
- [7] J. R. Camargo, L. O. Orzari, D. A. G. Araújo, P. R. de Oliveira, C. Kalinke, D. P. Rocha, A. Luiz dos Santos, R. M. Takeuchi, R. A. A. Munoz, J. A. Bonacin, B. C. Janegitz, Microchem. J. 2021, 164,
- [8] T. Kant, K. Shrivas, K. Dewangan, A. Kumar, N. K. Jaiswal, M. K. Deb, S. Pervez, Mater. Today Chem. 2022, 24, 100769.
- [9] A. Sharma, H. Faber, A. Khosla, T. D. Anthopoulos, Mater. Sci. Eng.: R: Rep. 2023, 156, 100754.
- [10] A. Ambrosi, M. Pumera, Chem. Soc. Rev. 2016, 45, 2740.
- [11] R. Ye, D. K. James, J. M. Tour, Adv. Mater. 2019, 31, 1803621.
- [12] M. Wang, Y. Yang, W. Gao, P. Cherng, Trends Chem 2021, 3, 969.
- [13] F. Silveri, F. Della Pelle, D. Compagnone, TrAC, Trends Anal. Chem. 2025. 185. 118175.
- [14] T. E. Benavidez, R. Martinez-Duarte, C. D. Garcia, Anal. Methods 2016,
- [15] A. Himani, T. Agarwal, Mater. Today Chem. 2025, 45, 102646.
- [16] J. Lin, Z. Peng, Y. Liu, F. Ruiz-Zepeda, R. Ye, E. L. G. Samuel, M. J. Yacaman, B. I. Yakobson, J. M. Tour, Nat. Commun. 2014, 5, 5714.
- [17] D. X. Luong, K. Yang, J. Yoon, S. P. Singh, T. Wang, C. J. Arnusch, J. M. Tour, ACS Nano 2019, 13, 2579.
- [18] W. R. de Araujo, C. M. R. Frasson, W. A. Ameku, J. R. Silva, L. Angnes, T. R. L. C. Paixão, Angew. Chem., Int. Ed. 2017, 56, 15113.
- [19] Y. Li, D. X. Luong, J. Zhang, Y. R. Tarkunde, C. Kittrell, F. Sargunaraj, Y. Ji, C. J. Arnusch, J. M. Tour, Adv. Mater. 2017, 29, 1700496.
- [20] Y. Chyan, R. Ye, Y. Li, S. P. Singh, C. J. Arnusch, J. M. Tour, ACS Nano 2018, 12, 2176.
- [21] S. Luo, P. T. Hoang, T. Liu, Carbon 2016, 96, 522.
- [22] F. M. Vivaldi, A. Dallinger, A. Bonini, N. Poma, L. Sembranti, D. Biagini, P. Salvo, F. Greco, F. Di Francesco, ACS Appl. Mater. Interfaces 2021, 13, 30245.
- [23] A. Nag, R. B. V. B. Simorangkir, D. R. Gawade, S. Nuthalapati, J. L. Buckley, B. O'Flynn, M. E. Altinsoy, S. C. Mukhopadhyay, Mater. Des. **2022**, 221, 110971.
- [24] X. Ruan, R. Wang, J. Luo, Y. Yao, T. Liu, Mater. Des. 2018, 160, 1168.
- [25] Y. Xu, Q. Fei, M. Page, G. Zhao, Y. Ling, D. Chen, Z. Yan, Nano Res. 2021, 14, 3033.
- [26] L. Huang, J. Su, Y. Song, R. Ye, Nanomicro Lett. 2020, 12, 157.
- [27] H. Yoon, J. Nah, H. Kim, S. Ko, M. Sharifuzzaman, S. C. Barman, X. Xuan, J. Kim, J. Y. Park, Sens. Actuators, B 2020, 311, 127866.

e01374 (9 of 10)

- [28] D. M. de Farias, L. A. Pradela-Filho, I. V. S. Arantes, J. L. M. Gongoni, W. B. Veloso, G. N. Meloni, T. R. L. C. Paixão, ACS Appl. Mater. Interfaces 2023, 15, 56424.
- [29] L. F. Mendes, A. de Siervo, W. Reis de Araujo, T. R. Longo, C. Paixão, Carbon 2020, 159, 110.
- [30] R. Murray, M. Burke, D. Iacopino, A. J. Quinn, ACS Omega 2021, 6,
- [31] L. X. Duy, Z. Peng, Y. Li, J. Zhang, Y. Ji, J. M. Tour, Carbon 2018, 126, 472
- [32] S. Wirojsaengthong, O. Chailapakul, P. Tangkijvanich, C. S. Henry, P. Puthongkham, Electrochim. Acta 2024, 494, 144452.
- [33] A. F. Carvalho, A. J. S. Fernandes, C. Leitão, J. Deuermeier, A. C. Marques, R. Martins, E. Fortunato, F. M. Costa, Adv. Funct. Mater. 2018, 28, 1805271.
- [34] T.-S. D. Le, H.-P. Phan, S. Kwon, S. Park, Y. Jung, J. Min, B. J. Chun, H. Yoon, S. H. Ko, S.-W. Kim, Y.-J. Kim, Adv. Funct. Mater. 2022, 32,
- [35] L. Kotthoff, S. Dey, J. Heil, V. Jain, T. Muller, A. Tyrrell, H. Wahab, P. Johnson, in Frontiers in Artificial Intelligence and Applications, IOS Press BV, Amsterdam, The Netherlands 2022, pp. 31.
- [36] A. Lamberti, F. Clerici, M. Fontana, L. Scaltrito, Adv. Energy Mater. **2016**, 6, 1600050.
- [37] E. R. Mamleyev, S. Heissler, A. Nefedov, P. G. Weidler, N. Nordin, V. V. Kudryashov, K. Länge, N. MacKinnon, S. Sharma, npj Flexible Electron. 2019. 3. 2.
- [38] S. P. Singh, Y. Li, A. Be'er, Y. Oren, J. M. Tour, C. J. Arnusch, ACS Appl. Mater. Interfaces 2017, 9, 18238.
- [39] F. Hasheminia, S. Sadeghzadeh, Nano-Struct. Nano-Objects 2024, 40,
- [40] A. K. Thakur, H. Mahbub, F. H. Nowrin, M. Malmali, ACS Appl. Mater. Interfaces 2022, 14, 46884.
- [41] Z. Zhang, M. Song, J. Hao, K. Wu, C. Li, C. Hu, Carbon N Y 2018, 127,
- [42] A. Behrent, C. Griesche, P. Sippel, A. J. Baeumner, Microchim. Acta 2021, 188, 159.
- [43] M. Devi, H. Wang, S. Moon, S. Sharma, V. Strauss, Adv. Mater. 2023, 35 2211054
- [44] M. Burke, C. Larrigy, E. Vaughan, G. Paterakis, L. Sygellou, A. J. Quinn, G. Herzog, C. Galiotis, D. Iacopino, ACS Omega 2020, 5,
- [45] R. L. McCreery, Chem. Rev. 2008, 108, 2646.
- [46] M. E. Sandison, N. Anicet, A. Glidle, J. M. Cooper, Anal. Chem. 2002, 74, 5717.
- [47] V. Strong, S. Dubin, M. F. El-Kady, A. Lech, Y. Wang, B. H. Weiller, R. B. Kaner, ACS Nano 2012, 6, 1395.
- [48] E. Vaughan, C. Santillo, M. Setti, C. Larrigy, A. J. Quinn, G. Gentile, M. Lavorgna, D. Iacopino, Advanced Sensor Research 2023, 2, 2300026.
- [49] T. Pinheiro, M. Morais, S. Silvestre, E. Carlos, J. Coelho, H. V. Almeida, P. Barquinha, E. Fortunato, R. Martins, Adv. Mater. 2024, 36, 2402014.
- [50] L. M. A. Ribeiro, D. J. Feria, P. C. Falcoswki, M. N. P. Carreño, I. Pereyra, M. Bertotti, J. Appl. Electrochem. 2024, 54,
- [51] J. Śmietańska, Spiral Length Calculator, Omni Calculator, available at: https://www.omnicalculator.com/math/spiral-length (accessed: Jan-
- [52] S. L. Silvestre, T. Pinheiro, A. C. Marques, J. Deuermeier, J. Coelho, R. Martins, L. Pereira, E. Fortunato, Flex. Printed Electronics 2022, 7, 035021.
- [53] A. Tiliakos, C. Ceaus, S. M. Iordache, E. Vasile, I. Stamatin, J. Anal. Appl. Pyrolysis 2016, 121, 275.
- [54] R. L. McCreery, Chem. Rev. 2008, 108, 2646.
- G.-F. Zhang, X. Liu, S. Zhang, B. Pan, M.-L. Liu, Eur. J. Med. Chem. [55] 2018, 146, 599,

www.advancedsciencenews.com

www.advmattechnol.de

- [56] K. Alagumalai, S. Palanisamy, P. S. Kumar, N. A. ElNaker, S.-C. Kim, M. Chiesa, P. Prakash, Environ. Pollution 2024, 343, 123189.
- [57] L. V. de Faria, D. M. de Farias, T. P. Lisboa, M. A. C. Matos, R. A. A. Munoz, R. C. Matos, Anal. Bioanal. Chem. 2022, 414, 5309.
- [58] K. Alagumalai, S. Palanisamy, P. S. Kumar, N. A. ElNaker, S.-C. Kim, M. Chiesa, P. Prakash, Environ. Pollution 2024, 343, 123189.
- [59] C. Liu, D. Xie, P. Liu, S. Xie, S. Wang, F. Cheng, M. Zhang, L. Wang, Microchim. Acta 2018, 186, 21.
- [60] D. M. de Farias, L. V. de Faria, T. P. Lisboa, M. A. C. Matos, R. A. A. Muñoz, R. C. Matos, J. Solid State Electrochem. 2020, 24,
- [61] G. N. Meloni, M. Bertotti, Electroanalysis 2017, 29, 787.

Adv. Mater. Technol. 2025, e01374